crystals

Article

Differential Frequency Exploration of Vortex Light in Lithium Niobate Crystals

Xing Wei [1,*], Samuel Kesse [2] and Ballipalli Chandra Babu [3]

1 Laser Technology New System Integration Innovation Center, Shanghai Institute of Optics and Fine Mechanics, Chinese Academy of Sciences, Shanghai 201800, China
2 School of Pharmacy, Shanghai Jiao Tong University, Shanghai 200240, China
3 Guangzhou Key Laboratory of Flexible Electronic Materials and Wearable Devices, School of Materials Science and Engineering, Sun Yat-Sen University, Guangzhou 510275, China
* Correspondence: DG1622042@smail.nju.edu.cn; Tel.: +86-15950472802

Abstract: In recent years, Orbital Angular Momentum (OAM) beams have been applied in optical communications to improve channel capacity and spectral efficiency. However, in practical applications, OAM information is often imprinted on short-wavelength light beams. How to completely transfer this information to the O-band to achieve long-distance transmission has not been conveniently achieved through most traditional methods. We studied the differential frequency experiment of OAM-carrying beams from both theoretical and experimental facets. In the periodic polarization 0 class matched lithium niobate crystal, the difference in frequency between the incident 1950 nm strong pump light and the 780 nm weak input light is achieved, resulting in output light in the O band. The polarization period of the crystal is 20 μm, and the best phase matching is achieved when the temperature is maintained at 41.2 °C. At this time, 780 nm vortex light produces 1300 nm vortex light, and the nonlinear conversion efficiency reaches 0.1387% (topological charge number l = 5). During the experiment, momentum, energy, and topological charge are all conserved. Our experiment successfully converted vortex light at 780 nm into vortex light at 1300 nm, paving the way for the subsequent conversion of 780 nm single photons generated by quantum dots carrying OAM into OAM photons in the communication band.

Keywords: OAM; vortex light; periodically poled lithium niobate crystals; differential frequency

Citation: Wei, X.; Kesse, S.; Babu, B.C. Differential Frequency Exploration of Vortex Light in Lithium Niobate Crystals. *Crystals* **2023**, *13*, 154. https://doi.org/10.3390/cryst13010154

Academic Editors: Bing-Yan Wei, Peng Chen, Haiwei Chen, Miao Jiang and Wan-Long Zhang

Received: 13 December 2022
Revised: 7 January 2023
Accepted: 9 January 2023
Published: 16 January 2023

1. Introduction

The vortex phase relationship of the spatial waveform is *exp (-ilθ)*, and the OAM of each photon is $l\hbar$, where θ is the azimuth coordinate of the transverse plane, and the integer l is the value of the topological charge. The unique characteristics related to OAM make this type of beam a subject that needs to be fully studied, and it has a variety of applications in micromanipulation, super-resolution imaging, and classical and quantum confidential communications [1–8]. In these studies, OAM exchange in nonlinear interactions is of particular interest. Through the frequency up-conversion [9–12] and down-conversion in nonlinear optical crystals [13,14], the four-wave mixing in atomic vapor [15,16], and the frequency conversion of higher harmonics in gaseous media [17,18], a beam of OAM carrying a new wavelength can be generated. In addition, by performing nonlinear frequency conversion of beams carrying OAM, the wavelength range of existing light sources can be widened. For example, high-order harmonics of gases can be used to generate beams carrying OAM [19]. The ultraviolet band can produce continuously adjustable mid- and far-infrared beams carrying OAM [20]. The important application of two-photon OAM quantum entanglement in the field of quantum information can be realized by using the process of spontaneous parametric down-conversion and four-wave mixing (signal light) [21,22].

In 1996, Allen et al. achieved the first frequency doubling of the LG (Laguerre-Gaussian) beam using lithium triborate crystals and potassium titanyl phosphate crystals. In the frequency doubling process satisfying the birefringence phase-matching condition, the OAM is conserved [23,24]. Afterwards, GK Samanda et al. used bismuth borate crystals to perform efficient frequency doubling of LG beams with large femtosecond topological charge numbers [25,26] and used barium metaborate crystals to generate ultraviolet (266 nm) carrying OAM beams [27]. In 2013, G. H. Shao et al., by solving the Periodically Poled Lithium Niobate (PPLN) crystal collinear quasi-phase-matching coupled wave equation, theoretically determined that the OAM of the harmonic is equal to the sum of the OAM of the fundamental wave, which satisfies the conservation of OAM [28]. In 2014, Z. Y. Zhou et al. used a Periodically Poled Potassium Titanyl Phosphate (PPKTP) crystal to realize the frequency doubling and sum-frequency of beams carrying OAM [29,30] and used the cavity enhancement effect to improve the frequency doubling conversion efficiency [31]. Many research groups have achieved frequency doubling, summation-frequency, differential frequency [32,33], triple frequency, quadruple frequency, Optical Parametric Amplifier (OPA) [34], and Optical Parametric Oscillator (OPO) [35–37] of beams carrying OAM during birefringent phase-matching or quasi-phase-matching. The OAM of photons is conserved in the process of nonlinear frequency conversion, and the spectral range carrying the OAM is broadened. OAM single-photon sources can be widely used in the fields of quantum communication [38], linear optical quantum computing, etc. [39–43]. OAM single-photon sources based on semiconductor quantum dots can also be used as a medium for connecting solid-state qubits in quantum dots [44,45], which is one of the important prerequisites for the realization of OAM single-photon-based solid-state quantum networks [46–49]. However, the wavelengths of the OAM single-photon sources of semiconductor quantum dots are concentrated in the range usually near 780 nm and 900 nm. By using the nonlinear effect of lithium niobate crystal, narrow bandwidth vortex light can be generated in the O-band, which can not only broaden the wavelength range of the OAM single-photon source, but also realize the entanglement exchange of a photon in the 780 nm quantum dot entanglement source carrying OAM into a 1300 nm OAM photon. In addition, photons carrying OAM can carry more information as well as control the angular momentum entanglement of photons, which plays a very significant role in quantum communication and quantum coding. Selecting the angular momentum and projection basis vector of crystals can achieve high-order angular momentum entanglement, which is used to improve angular resolution in quantum remote sensing technology.

In the experiment, the vortex light in the communication band is generated by the different frequency processes of the OAM-carrying input light and the Gaussian pump light in the periodically poled lithium niobate crystal. The topological charges of the input light are selected to be 5, 3, 2, and 1, and the coupling period of the nonlinear process is appropriately designed to achieve the best quasi-phase-matching. Vortex light with a spectral width of 0.06 nm can be obtained at approximately 1300 nm. The conversion efficiency is as high as 0.1387%. The topological charge is found to be conserved during nonlinear interactions. The experiment lays a solid foundation for the next step to convert photons generated by OAM-carrying 780 nm quantum dots into OAM single-photon sources with narrow linewidth in the communication band.

2. Results and Discussion

Theoretical Analysis. According to Maxwell's system of equations, the nonlinear fluctuation equation can be obtained under the condition of an approximate near-axis:

$$\nabla^2 A(r) + \varepsilon \frac{\omega^2}{c^2} A(r) = -\frac{\omega^2}{\varepsilon_0 c^2} P^{NL}(r) \tag{1}$$

where ε is the dielectric constant, P^{NL} is the polarization intensity in a nonlinear medium, and $A(r)$ is the electric field intensity vector. Under the approximation condition of the deceleration envelope, the nonlinear coupled wave Equation (1) solved numerically is as follows:

$$\frac{dA_{1z}}{dx} = -iKA_{2z}A_{3z}e^{-i\Delta kx} \tag{2}$$

$$\frac{dA_{2z}}{dx} = -iKA_{3z}^{*}A_{1z}e^{i\Delta kx} \tag{3}$$

$$\frac{dA_{3z}}{dx} = -iK^{*}A_{1z}A_{2z}^{*}e^{-i\Delta kx} \tag{4}$$

Here, A_{iz} (i = 1,2,3) is the z-direction amplitude of the pump, input and output respectively. In addition, K is among Equations (2)–(4), and the conversion efficiency of the differential frequency process in the periodically poled lithium niobate crystal can be obtained. The input wave is z-polarized and propagates along the x-axis of the nonlinear crystal. Here, ω_1, ω_2, and ω_3 represent the frequency of pump, input, and output light, respectively. $\Delta k = k_3 - k_1 - k_2$ represents the phase mismatch of the pump, input and output light respectively. According to Equations (2)–(4), the theoretical efficiency of the nonlinear transformation of the PPLN differential frequency experiment can be calculated [50]

$$\eta = \frac{P_3}{P_1} = \frac{8\pi^2 d_{eff}^2 L^2 P_2}{\varepsilon_0 c n_1 n_2 n_3 \lambda_1^2 S} sinc^2(|\Delta K| L/2). \tag{5}$$

Here, d_{eff} is the effective nonlinear coefficient of the crystal and k is the wave vector, $\Delta K = k_3 - k_1 - k_2$ represents the phase mismatch of the pump, input and output light respectively. $\varepsilon_0 = 8.854 \times 10^{-12}\mathrm{A{\cdot}s/(V \cdot m)}$ and $c = 3 \times 10^8$ m/s are the vacuum dielectric constant and the speed of light, λ_1 is the pump light wavelength, L is the length of the crystal, and P_1, P_2, and P_3 are the light power of the pump, input and output, respectively. S is the overlapping area between the pump light and the input light, and n_1, n_2, and n_3 are the refractive index of the pump, input and output light respectively. In addition, to facilitate the introduction of parameter calculation Equation (5), some parameters adopt the following dimensions: $\left[d_{eff}\right] = m/V; [P_2] = W; [L] = m; [S] = m^2; [\lambda] = m.$

From Equation (5), it can be seen that the nonlinear conversion efficiency of vortex light is related to the power density $\frac{P_2}{S}$ of the spot, and the power density $\frac{P_2}{S}$ gradually decreases as the topological charge number increases.

From the previous introduction to the OAM beam, we can simply express the spatial distribution of the OAM beam as $A_i(r, \phi, x) = E_i(x)u_i(r, x)e^{ik_i x}e^{il\phi}e^{-i(2p+l+1)\wp_i(x)}, (i = 1, 2, 3)$. The expressions represent the transverse electric field of the pump, input, and output lights, respectively. Here, $E_i(x)$ is the field amplitude, $u_i(r, x)$ is the transverse light field distribution, l is the topological charge number, k_i is the wave vector, and ϕ is the phase of the vortex light. $(2p + l + 1)\wp(x)$ represents the gouy phase, considering that $\wp_1(x) = \wp_2(x)$ and $\wp_1(x) \approx \wp_3(x)$ when p = 0, and it is brought into the coupled wave equation. Equations (2)–(4) obtain the topological charge transfer in the three-wave nonlinear process [30]:

$$\frac{dA_1}{dx} = -iKA_3A_2e^{-i\Delta kx}e^{i(l_2-l_3)\phi} \tag{6}$$

$$\frac{dA_2}{dx} = -iKA_1A_3^{*}e^{-i\Delta kx}e^{i(l_3+l_1)\phi} \tag{7}$$

$$\frac{dA_3}{dx} = -iK^{*}A_1A_2^{*}e^{-i\Delta kx}e^{i(l_2-l_1)\phi} \tag{8}$$

The $e^{il\varphi}$ can be expressed as the distribution of OAM. Usually, in the nonlinear transformation process, if there is no phase mismatch, $\Delta k = k_3 - k_1 - k_2 - G_{QPM} = 0$ (G_{QPM}) is the inverse lattice vector brought by quasi-phase-matching); at this time, the value of $e^{il\varphi}$ in the coupled wave equation is constant l. Combining the coupled wave Equations (5)–(7), the topological charge number of the input light in the differential frequency process is $l_2 = l_3 + l_1$, and the frequency of the output light is $\omega_3 = \omega_1 - \omega_2$.

In summary, during the nonlinear conversion process of the beam carrying OAM, it is necessary not only to satisfy the conservation of momentum in the transmission direction but also to satisfy the conservation of OAM. The conservation relationship of OAM in the nonlinear matching process is only established without phase mismatch. If you consider the effects of mismatch, a discrete map can be obtained (the term "discrete map" indicates that the orbital angular momentum is not conserved).

3. Experiment Results

Our experimental sample is a periodically poled lithium niobate crystal with a length of 50 mm, and a width and height of 1 mm. The polarization period along the y-axis is 20 µm, with a total of 2500 polarization cycles. The schematic diagram is shown in Figure 1. G_{QPM} represents the inverted lattice vector, which is the polarization period of the crystal. Figure 1a shows the energy conservation of the nonlinear process. Figure 1b,c shows a schematic diagram of the conversion of the 1950 nm Gaussian-distributed pump light and 780 nm input light into 1300 nm vortex light. This shows that the inverted lattice vector of the crystal compensates for the phase mismatch of the three waves during the nonlinear conversion process so that the pump light and the input light are continuously converted into output light.

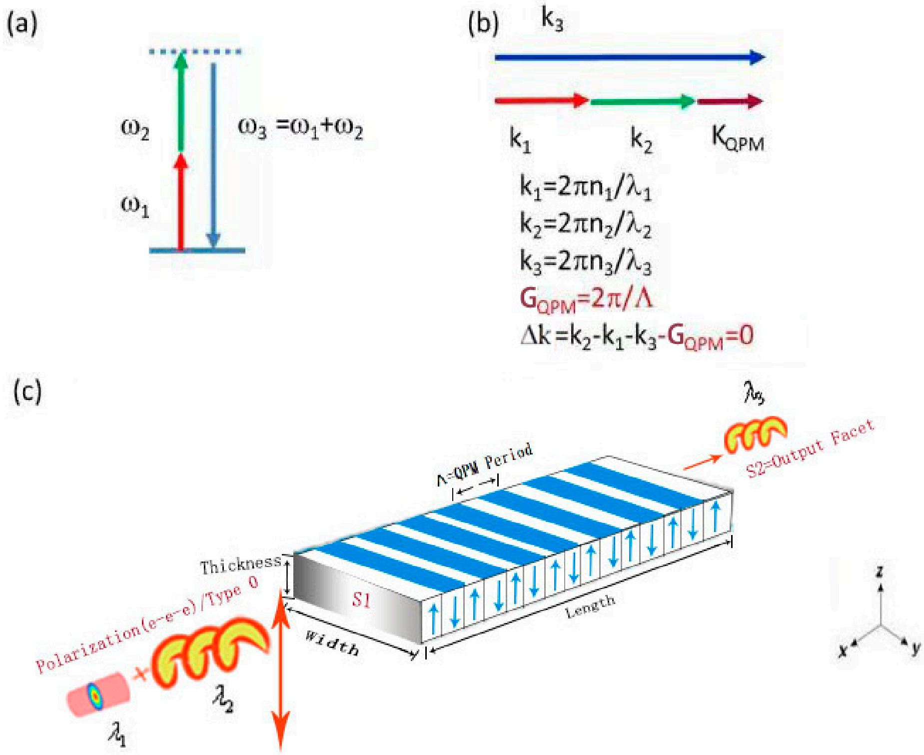

Figure 1. Schematic diagram of the experiment. (**a**) Photon Energy Conservation. (**b**) Photon Momentum Conservation. (**c**) Periodically reverse domain with Period∧, which creates wave vector G_{QPM} == 2/∧for the quasi-phase-matching (QPM) interaction.

The experimental optical path diagram is shown in Figure 2. The key optical components (abbreviations) of the optical path include the collimator, half-wave plate (HWP), periodically poled lithium niobate (PPLN) (the length of the crystal set to 50.0 mm, height 1.0 mm, and width 12.3 mm), polarization beam splitter (PBS), quarter-wave plate (QWP), camera (CCD), baffle (Baffle), filter (Filter), mirror (M), lens (L1–L4) (f_1 = 100 mm, f_2 = 60 mm, f_3 = 45 mm, f_4 = 45 mm) and spatial light modulator (SLM). The incident 780 nm input light with a line width of 2 kHz is obtained by a continuous laser of 1560 nm and a frequency doubling (frequency quasi-laser) of a PPLN crystal. The 780 nm laser is emitted horizontally polarized through the polarization controller and then incident through the collimator to the spatial light modulator (UPOLabs, HDSLM80R) for reflection. This process converts the Gaussian beam into vortex light with topological charge numbers $l = 5, 3, 2$, and 1. The 780 nm laser passes through the SLM and then passes through the combination of HWP and QWP. The SLM is to generate vortex light with different topological charges, and the combination of HWP and QWP is to adjust the light intensity of the vortex light incident on the PPLN crystal to obtain different nonlinearity conversion efficiency. The polarization of the vortex input light is parallel to the z-axis of the periodically poled lithium niobate crystal to take advantage of the maximum nonlinearity coefficient d_{33}. After the 780 nm laser passes through the SLM, the spot is relatively large, and it needs to be compressed by two convex lens groups with focal lengths of 100 mm and 60 mm, and the two lenses are separated by 18 cm. Next, an achromatic lens with a focusing length of 45 mm is used to focus the input light and the pump light into a nonlinear crystal. Due to the action of the lens, the girdle radii of the input light and the pump light in the centre of the crystal are 80 μm and 70 μm, respectively, and the power intensity in the crystal is approximately 0.87 kW/cm^2. The wavelength of the strong pump light is 1950 nm, and the line width is 10 kHz. The lithium niobate crystals were placed in a temperature-controlled furnace, and the crystal temperature was maintained at 41.2 °C. The emitted light at the end of the crystal first passes through an achromatic lens with a focal length of 45 mm and then passes through two filters. Filters 1 and 2 filter out the input light and the pump light, respectively. The resulting 1300 nm vortex beam is monitored by a CCD camera. In addition, the 1300 nm light spot directly seen by the CCD is close to a circular ring. To measure the topological charge, we use a cylindrical lens with a focal length of 20 mm, a width of 10 mm and a length of 20 mm for compression.

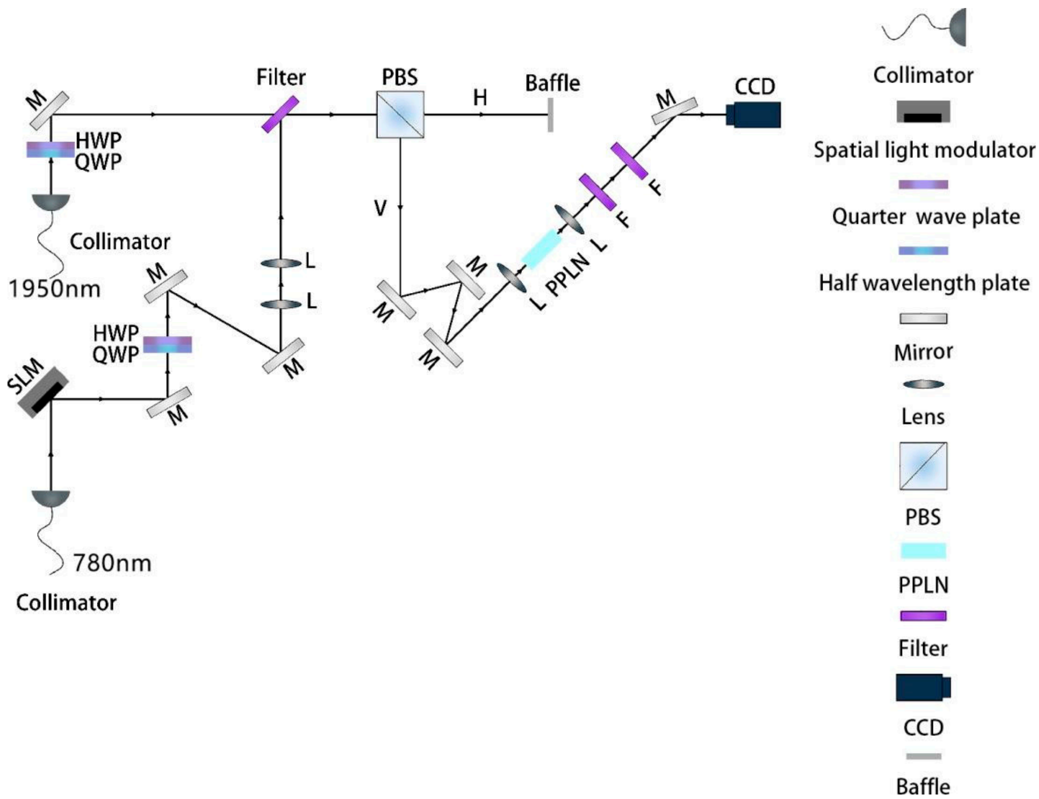

Figure 2. Experimental optical path diagram showing the helical phase profile loaded on the SLM to generate vortices. Key components (abbreviations) include combiner, half-wave plate (HWP), PPLN, PBS, quarter-wave plate (QWP), CCD, baffle, filter, mirror (M), lens (L1–L4), and spatial light modulator (SLM).

Based on theoretical analysis and modelling, we simulated the light intensity distribution of input light with different topological loads. Figure 3 shows the light intensity evolution and phase distribution during the propagation of the vortex light field. To obtain more accurate results, we chose different topological loads for testing and used a circular cylindrical lens to measure the topological loads of output light (the topological loads can be obtained by calculating the number of dark stripes in the focusing pattern). Here, we present the measurement results of the simulation and experiment. Figure 3f,k,p experimental device diagrams show the spiral phase contours loaded on the SLM to produce eddy currents. Figure 3b,g,l,q are the results of theoretical calculations, which accurately simulate the transverse light field distribution of the light field carrying l = 5, 3, 2, 1. Figure 3c,d,h,i,m,n,r,s represent the horizontal light field distribution map of the input light and output light recorded on the CCD camera when the topological load l = 5, 3, 2, 1 input and output light fields Figure 3c,h,m,r show the distribution of the input light fields. In addition, Figure 3d,i,n,s represents the distribution of the output light fields). From Figure 3d,i,n,s, the lateral structure of the spot is distorted, because of the overlapping area of (1). 1950 nm laser and 780 nm laser do not reach the optimal position. (2). The 1300 nm laser passes through the lens, two filters and optical elements, resulting in the distortion of the spot. Figure 3e,j,o,t contains a transverse light field distribution map of the emitted light field after the 1300 nm laser with l = 5, 3, 2, 1 is compressed through the cylindrical lens. From the figure, we can see that when the topological loads of the input light are 5, 3, 2, and 1, the incident spot maintains an annular intensity distribution. The topological loads loaded on the input light are equal to the topological loads of the 1300 nm vortex light generated. A cylindrical lens is used to convert OAM light into the Laguerre-Gaussian mode [51,52]. The number of dark stripes of the compressed spot is the number of topological charges. By calculating Figure 3e,j,o, the dark stripes shown in Figure 3t show that when the topological charge of 780 nm light is 5, the number of dark stripes that output 1300 nm light is 5, that is, the topological charge is 5, which confirms the law of conservation of topological charge during nonlinear frequency conversion. In addition, we define the ratio of the modulated part of the output light to the incident light as the reflection efficiency. When holograms are generated on the SLM, the reason why the reflection efficiency of the SLM decreases with the increase of topological charge is that there is a part of the light reflected through the SLM that is modulated and a part that is not modulated. As the topological charge increases to a certain order, the modulated part decreases gradually. Table 1 shows the experimental and simulation data of the output power of the output light under different topological charges and different pump power conditions. Then, according to Equation (5) and the experimental results, the nonlinear transformation is calculated theoretical efficiency. When the beam waist radius of the input light and the pump light is 80 μm and 70 μm, respectively, the incident pump power is kept at 180 mW, and the actual output power of the crystal measured in the experiment gradually decreases with increasing topological charge. The results are shown in Figure 4. We solved the coupling fluctuation equation numerically and calculated the theoretical and experimental values of the conversion efficiency of the DFG process based on a series of parameters of the periodic polarization structure used in the experiment. The theoretical simulation calculation results are consistent with the trend of the experimental results. As shown in Figure 4, the emission power of output light decreases with increasing topological charge (inferred from Equation (5)). This is because the overlap integral between the pump light and the input light decreases with increasing topological charge, decreasing spot area and the energy density of the spot decreases. In addition, by changing the temperature of the PPLN crystal, the tunable DFG in the periodically poled lithium niobate crystal was experimentally studied. Figure 4 shows the experimental and theoretical emission power of output light in the DFG process, which depends on the topological load of the input light. The nonlinear conversion efficiency reaches 0.1387% (the nonlinear conversion efficiency is equal to the power of output light divided by the power of the input light). At this time, the power of the incident input light is 6 mW, the 1950 nm laser power is 180 mW, and the 1300 nm vortex light power is 8.326 μW. Table 1 for specific values. In addition, the theoretical ghost area S and the topological charge of the 1950 nm and 780 nm laser spots are also related to the overlap integral, and decrease with the increase of the topological charge. We can get the efficiency of theoretical calculation by substituting all the parameters such as $k_i = \frac{2\pi}{\lambda_i}, L = 50$ mm, $P_2 = 6$ mW, $P_3 = 180$ mW, $n_1 = 2.1983, n_2 = 2.258, n_3 = 2.2204$ into Equation (5). The experimental data in Table 1 and Figure 4 are all the output light tested under the condition that the pump optical power and the input optical power remain unchanged. The output power and efficiency of light. With the change of topological charge, the ghost area of the 1950 nm laser and 780 nm laser is different. In addition to the limitation of experimental conditions, the laser spot of 1950 nm and 780 nm we adjusted may not always be the largest weight. Therefore, the output power of the 1300 nm laser, as well as the theoretical and experimental nonlinear conversion efficiencies vary greatly and there are certain errors, but the general trend is the same.

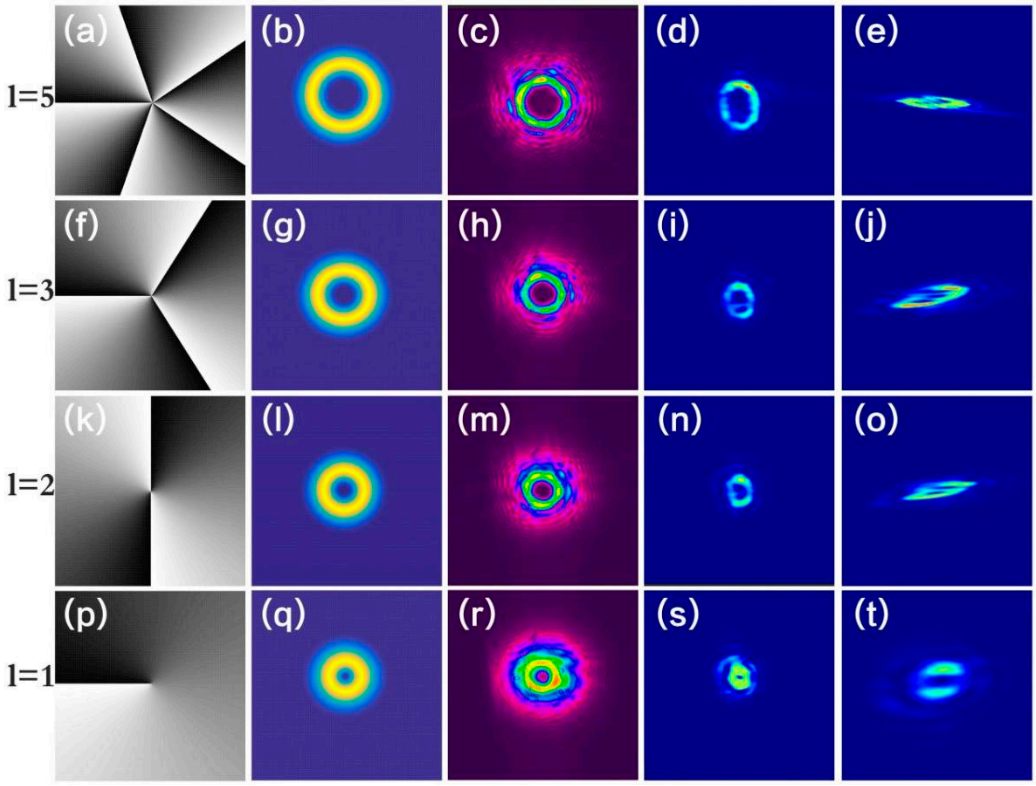

Figure 3. Light intensity distribution and phase distribution during propagation of the vortex optical field. (**a**,**f**,**k**,**p**) Spiral phase diagrams of different topological charges loaded by spatial light modulators. (**b**,**g**,**l**,**q**) are the theories that accurately model the lateral light field distributions carrying light fields of l = 5, 3, 2, 1. (**c**,**d**,**h**,**i**,**m**,**n**,**r**,**s**) represent the input and output light fields with topological charge L = 5, 3, 2, 1 (**c**,**h**,**m**,**r**) show the distribution of the input light fields. In addition, (**d**,**i**,**n**,**s**) represent the distribution of the output light fields). The lateral light field distribution maps of (**e**,**j**,**o**,**t**) are the lateral light field structures of the output light field after being compressed by a cylindrical lens carrying a 1300 nm laser with l = 5, 3, 2, 1. (**a**,**b**,**f**,**g**,**k**,**l**,**p**,**q**) are numerical simulation graphs, and (**c**,**d**,**e**,**h**,**i**,**j**,**m**,**n**,**o**,**r**,**s**,**t**) are experimental results.

Table 1. The experimental and theoretical output power of output light as a function of the topological charge of vortex light at 780 nm, where the pump power at 1950 nm is 180 mW and the power at 780 nm is 6 mW.

Topological Charge	Power (μW)	Theoretical Efficiency
1	8.32	90%
2	3.61	39%
3	2.50	28%
5	0.52634	5.8%

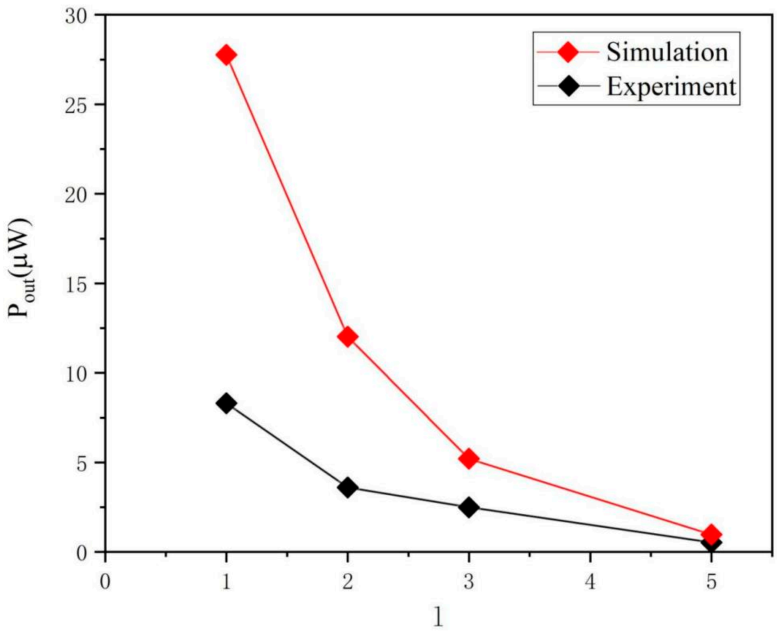

Figure 4. The experimental and theoretical output power of output light as a function of the topological charge of vortex light at 780 nm, where the pump power at 1950 nm is 180 mW and the power at 780 nm is 6 mW.

There is a certain deviation between the theoretical and experimental values corresponding to the output frequency optical output power of different topological loads shown in Figure 4 (The data in Figure 4 shows that the incident power of the fixed 1950 nm pump is 180 mW, and the incident light power of 780 nm is 6 mW. Under the conditions of 780 nm incident light with different topological charges, the experimentally measured output light power of 1300 nm.). The reason is that the reflection of the crystal end face, the filter loss, and the length of the periodic polarization are not strictly matched. The optimization of the experiment requires a 1950 nm beam spot meter to adjust the size of the spot to maximize the overlap between the input light and the pump light to further improve the nonlinear conversion efficiency. The current efficiency cannot achieve the efficient conversion of vortex photons generated by quantum dots of 780 nm. Next, the conversion efficiency will be further improved, and low-crosstalk quantum integrated chips and devices carrying OAM will be made for the multiplexing and transmission of optical quantum information and OAM optical communication systems [53]. The wavelengths of all the output light in the paper are measured by an OSA spectrometer, which is determined to be around 1300 nm. Figure 5 is the spectrogram of the output light, with the peak value of the output wavelength around 1300.537 nm.

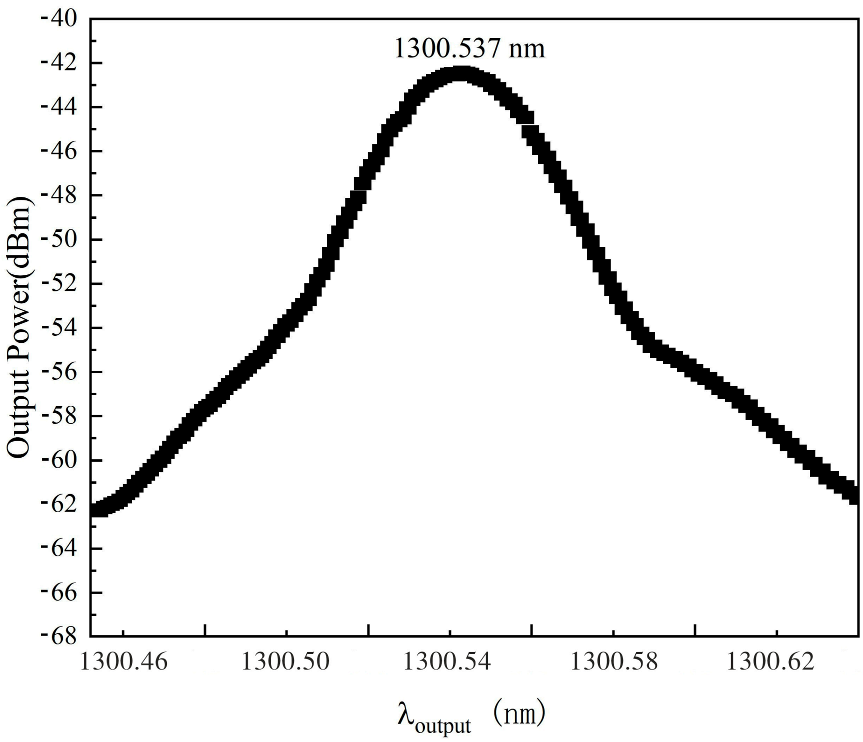

Figure 5. The figure shows the spectrum of the outgoing light, with the peak value of the output wavelength around 1300.537 nm.

4. Conclusions

In this work, a scheme for converting nonvortex light into vortex light by periodically poled lithium niobate crystals is proposed. In PPLN, we use 780 nm vortex light with topological charge numbers of 5, 3, 2, and 1 and a strong laser with a Gaussian distribution of 1950 nm to realize the nonlinear effect of the difference frequency and efficiently output 1300 nm vortex light. The polarization period of the lithium niobate crystal is 20 μm, and the temperature of the lithium niobate crystal is changed. When it reaches 41.2 °C, the crystal achieves the best phase matching. During the experiment, the momentum, energy, and topological charge of the pump, input, and output lights were conserved. Because the 1950 nm laser is Gaussian distributed, the topological charge of the 1300 nm vortex light is equal to the topological charge of the 780 nm vortex light. The experiment measured that the half-height and full-width of the 1300 nm vortex light produced was 0.06 nm. Our experiment paves the way for the conversion of a 780 nm single photon carrying OAM into a narrow linewidth OAM single photon in the communication band.

Author Contributions: X.W. designed the experiment project. X.W. performed the analysis of the effective theoretical model and experiment results. X.W. supervised the project. X.W. wrote the manuscript with input from all authors. X.W., S.K. and B.C.B. revised the paper and suggested some revisions. All authors have read and agreed to the published version of the manuscript.

Funding: This work was funded by the Fundamental Research Funds for the Central Universities and the National Supercomputer Center in Guangzhou; the National Key R&D Program of China (2018YFA0306100); the National Natural Science Foundation of China (11874437 and 61935009); the Guangzhou Science and Technology Project (201805010004); and the Natural Science Foundation of Guangdong (2018B030311027, 2016A030306016, and 2016TQ03X981).

Institutional Review Board Statement: Not applicable.

Informed Consent Statement: Not applicable.

Data Availability Statement: The datasets used and/or analysed during the current study are available from the corresponding author upon reasonable request.

Conflicts of Interest: The authors declare no conflict of interest.

References

1. Paterson, L.; MacDonald, M.P.; Arlt, J.; Sibbett, W.; Bryant, P.E.; Dholakia, K. Controlled rotation of optically trapped microscopic particles. *Science* **2001**, *292*, 912–914. [CrossRef] [PubMed]
2. O'neil, A.T.; MacVicar, I.; Allen, L.; Padgett, M.J. Intrinsic and extrinsic nature of the orbital angular momentum of a light beam. *Phys. Rev. Lett.* **2002**, *88*, 053601. [CrossRef]
3. Yu, W.; Ji, Z.; Dong, D.; Yang, X.; Xiao, Y.; Gong, Q.; Xi, P.; Shi, K. Super-resolution deep imaging with hollow Bessel beam STED microcopy. *Laser Photonics Rev.* **2016**, *10*, 147–152. [CrossRef]
4. Gibson, G.; Courtial, J.; Padgett, M.J.; Vasnetsov, M.; Pas'ko, V.; Barnett, S.M.; Franke-Arnold, S. Free-space information transfer using light beams carrying orbital angular momentum. *Opt. Express* **2004**, *12*, 5448–5456. [CrossRef] [PubMed]
5. Wang, J.; Yang, J.Y.; Fazal, I.M.; Ahmed, N.; Yan, Y.; Huang, H.; Ren, Y.; Yue, Y.; Dolinar, S.; Tur, M.; et al. Terabit free-pace data transmission employing orbitl angular mmentum multiplexing. *Nat. Photonics* **2012**, *6*, 488–496. [CrossRef]
6. D'ambrosio, V.; Spagnloon, N.; Del Re, L.; Slussarenko, S.; Li, Y.; Kwek, L.C.; Marrucci, L.; Walborn, S.P.; Aolita, L.; Sciarrino, F. Photonic parization gears for ultra-ensitive angular measurements. *Nat. Commun.* **2013**, *4*, 2432.
7. Lavery, M.P.J.; Speirits, F.C.; Barnett, S.M.; Padgett, M.J. Detection of a spinning object using light's orbital angular momentum. *Science* **2013**, *341*, 537–540. [CrossRef]
8. Nagali, E.; Sciarrino, F.; De Martini, F.; Marrucci, L.; Piccirillo, B.; Karimi, E.; Santamato, E. Quantum information transfer from spin to the orbital angular momentum of photons. *Phys. Rev. Lett.* **2009**, *103*, 013601. [CrossRef]
9. Ou, Z.Y.; Mandel, L. Violation of Bell's inequality and classical probability in a two-photon correlation experiment. *Physical Rev. Lett.* **1988**, *61*, 50. [CrossRef]
10. Li, X.; Voss, P.L.; Sharping, J.E.; Kumar, P. Optical-fiber source of polarization-entangled photons in the 1550 nm telecom band. *Phys. Rev. Lett.* **2005**, *94*, 053601. [CrossRef] [PubMed]
11. Liu, L.; Wang, H.; Ning, Y.; Zhao, L.; Zhao, W.; Guo, C.; Ren, G. Upconversion of communication band light carrying orbital angular momentum using quasi-phase-matching. In Proceedings of the Tenth International Conference on Information Optics and Photonics, Beijing, China, 8–11 July 2018.
12. Ge, Z.; Zhou, Z.Y.; Li, Y.; Yang, C.; Liu, S.K.; Shi, B.S. Fourth-harmonic generation of orbital angular momentum light with cascaded quasi-phase matching crystals. *Opt. Lett.* **2021**, *46*, 158–161. [CrossRef] [PubMed]
13. Petrov, V. Frequency down-conversion of solid-state laser sources to the mid-infrared spectral range using non-oxide nonlinear crystals. *Prog. Quantum Electron.* **2015**, *42*, 1–106. [CrossRef]
14. Christ, A.; Brecht, B.; Mauerer, W.; Silberhorn, C. Theory of quantum frequency conversion and type-II parametric down-conversion in the high-gain regime. *New J. Phys.* **2013**, *15*, 053038. [CrossRef]
15. Pan, X.; Yu, S.; Zhou, Y.; Zhang, K.; Zhang, K.; Lv, S.; Li, S.; Wang, W.; Jing, J. Orbital-angular-momentum multiplexed continuous-variable entanglement from four-wave mixing in hot atomic vapor. *Phys. Rev. Lett.* **2019**, *123*, 070506. [CrossRef] [PubMed]
16. Hu, H.; Luo, D.; Chen, H. Nonlinear frequency conversion of vector beams with four-wave mixing in atomic vapor. *Appl. Phys. Lett.* **2019**, *115*, 211101. [CrossRef]
17. Knyazev, B.A.; Serbo, V.G. Beams of photons with nonzero projections of orbital angular momenta: New results. *Phys. -Uspekhi* **2018**, *61*, 449. [CrossRef]
18. Bethune, D.; Rettner, C. Optical harmonic generation in nonuniform gaseous media with application to frequency tripling in free-jet expansions. *IEEE J. Quantum Electron.* **1987**, *23*, 1348–1360. [CrossRef]
19. Ribič, P.R.; Gauthier, D.; De, N.G. Generation of coherent extreme-ultraviolet radiation carrying orbital angular momentum. *Phys. Rev. Lett.* **2014**, *112*, 203602. [CrossRef]
20. van den Heuvel, F.C. Far-Infrared Spectroscopy with a Tunable Source of Radiation. Ph.D. Thesis, Radboud University Nijmegen, Nijmegen, The Netherlands, 1982.
21. Molina-Terraza, G.; Torres, J.P.; Torner, L. Twisted photons. *Nat. Phys.* **2007**, *3*, 305–310. [CrossRef]
22. Zhang, C.; Huang, Y.F.; Liu, B.H.; Li, C.F.; Guo, G.C. Spontaneous Parametric Down-Conversion Sources for Multiphoton Experiments. *Adv. Quantum Technol.* **2021**, *4*, 2000132. [CrossRef]
23. Dholakia, K.; Simpson, N.B.; Padgett, M.J.; Allen, L. Second-harmonic generation and the orbital angular momentum of light. *Phys. Rev. A* **1996**, *54*, R3742. [CrossRef]
24. Courtial, J.; Dholakia, K.; Allen, L.; Padgett, M.J. Second-harmonic generation and the conservation of orbital angular momentum with high-order Laguerre-Gaussian modes. *Phys. Rev. A* **1997**, *56*, 4193. [CrossRef]
25. Lesparre, F.; Gomes, J.T.; Délen, X.; Martial, I.; Didierjean, J.; Pallmann, W.; Resan, B.; Eckerle, M.; Graf, T.; Ahmed, M.A.; et al. High-power Yb: YAG single-crystal fiber amplifiers for femtosecond lasers in cylindrical polarization. *Opt. Lett.* **2015**, *40*, 2517–2520. [CrossRef] [PubMed]
26. Chaitanya, N.A.; Jabir, M.V.; Banerji, J.; Samanta, G.K. Hollow Gaussian beam generation through nonlinear interaction of photons with orbital angular momentum. *Sci. Rep.* **2016**, *6*, 32464. [CrossRef] [PubMed]
27. Chaitanya, N.A.; Kumar, S.C.; Devi, K.; Samanta, G.K.; Ebrahim-Zadeh, M. Ultrafast optical vortex beam generation in the ultraviolet. *Opt. Lett.* **2016**, *41*, 2715–2718. [CrossRef] [PubMed]

28. Shao, G.; Wu, Z.; Chen, J.; Xu, F.; Lu, Y. Nonlinear frequency conversion of fields with orbital angular momentum using quasi-phase-matching. *Phys. Rev. A* **2013**, *88*, 063827. [CrossRef]
29. Zhou, Z.Y.; Ding, D.S.; Jiang, Y.K.; Li, Y.; Shi, S.; Wang, X.S.; Shi, B.S. Orbital angular momentum light frequency conversion and interference with quasi-phase matching crystals. *Opt. Express* **2014**, *22*, 20298–20310. [CrossRef]
30. Li, Y.; Zhou, Z.Y.; Ding, D.S.; Shi, B.S. Sum frequency generation with two orbital angular momentum carrying laser beams. *JOSA B* **2015**, *32*, 407–411. [CrossRef]
31. Zhou, Z.Y.; Li, Y.; Ding, D.S.; Zhang, W.; Shi, S.; Shi, B.S.; Guo, G.C. Highly efficient second-harmonic generation of a light carrying orbital angular momentum in an external cavity. *Opt. Express* **2014**, *22*, 23673–23678. [CrossRef]
32. Bagmanov, V.K.; Sultanov, A.K.; Gizatulin, A.R.; Meshkov, I.K.; Kuk, I.A.; Grakhova, E.P.; Abdrakhmanova, G.I.; Bagmanov, V.K.; Sultanov, A.K.; Gizatulin, A.R.; et al. The vortex beams conversion from the optical range into the radio domain based on the nonlinear generation of the difference frequency. In Proceedings of the 2019 27th Telecommunications Forum (TELFOR), Belgrade, Serbiam, 26–27 November 2019; IEEE: Toulouse, France, 2019; pp. 1–4.
33. Miyamoto, K.; Sano, K.; Miyakawa, T.; Niinomi, H.; Toyoda, K.; Vallés, A.; Omatsu, T. Generation of high-quality terahertz OAM mode based on soft-aperture difference frequency generation. *Opt. Express* **2019**, *27*, 31840–31849. [CrossRef]
34. Fang, X.; Yang, H.; Zhang, Y.; Xiao, M. Optical parametric amplification of a Laguerre–Gaussian mode. *OSA Contin.* **2019**, *2*, 236–243. [CrossRef]
35. Camper, A.; Park, H.; Lai, Y.H.; Kageyama, H.; Li, S.; Talbert, B.K.; Blaga, C.I.; Agostini, P.; Ruchon, T.; DiMauro, L.F. Tunable mid-infrared source of light carrying orbital angular momentum in the femtosecond regime. *Opt. Lett.* **2017**, *42*, 3769–3772. [CrossRef] [PubMed]
36. Aadhi, A.; Samanta, G.K.; Chaitanya Kumar, S.; Ebrahim-Zadeh, M. Controlled switching of orbital angular momentum in an optical parametric oscillator. *Optica* **2017**, *4*, 349–355. [CrossRef]
37. Aadhi, A.; Sharma, V.; Samanta, G.K. High-power, continuous-wave, tunable mid-IR, higher-order vortex beam optical parametric oscillator. *Opt. Lett.* **2018**, *43*, 2312–2315. [CrossRef]
38. Chen, B.; Wei, Y.; Zhao, T.; Liu, S.; Su, R.; Yao, B.; Yu, Y.; Liu, J.; Wang, X. Bright solid-state sources for single photons with orbital angular momentum. *Nat. Nanotechnol.* **2021**, *16*, 302–307. [CrossRef]
39. Kok, P.; Munro, W.J.; Nemoto, K.; Ralph, T.C.; Dowling, J.P.; Milburn, G.J. Linear optical quantum computing with photonic qubits. *Rev. Mod. Phys.* **2007**, *79*, 135. [CrossRef]
40. Stav, T.; Faerman, A.; Maguid, E.; Oren, D.; Kleiner, V.; Hasman, E.; Segev, M. Quantum entanglement of the spin and orbital angular momentum of photons using metamaterials. *Science* **2018**, *361*, 1101–1104. [CrossRef]
41. Wang, X.L.; Luo, Y.H.; Huang, H.L.; Chen, M.C.; Su, Z.E.; Liu, C.; Chen, C.; Li, W.; Fang, Y.-Q.; Jiang, X.; et al. 18-Qubit entanglement with six photons' three degrees of freedom. *Phys. Rev. Lett.* **2018**, *120*, 260502. [CrossRef]
42. Fushman, I.; Englund, D.; Faraon, A.; Stoltz, N.; Petroff, P.; Vuckovic, J. Controlled Phase Shifts with a Single Quantum Dot. *Science* **2008**, *320*, 769–772. [CrossRef]
43. Strain, M.J.; Cai, X.; Wang, J.; Zhu, J.; Phillips, D.B.; Chen, L.; Lopez-Garcia, M.; O'Brien, J.L.; Thompson, M.G.; Sorel, M.; et al. Fast electrical switching of orbital angular momentum modes using ultra-compact integrated vortex emitters. *Nat. Commun.* **2014**, *5*, 4856. [CrossRef]
44. Miao, P.; Zhang, Z.; Sun, J.; Walasik, W.; Longhi, S.; Litchinitser, N.M.; Feng, L. Orbital angular momentum microlaser. *Science* **2016**, *353*, 464–467. [CrossRef] [PubMed]
45. Zhang, J.; Sun, C.; Xiong, B.; Wang, J.; Hao, Z.; Wang, L.; Han, Y.; Li, H.; Luo, Y.; Xiao, Y.; et al. An InP-based vortex beam emitter with monolithically integrated laser. *Nat. Commun.* **2018**, *9*, 2652. [CrossRef] [PubMed]
46. Yilmaz, S.T.; Fallahi, P.; Imamoğlu, A. Quantum-Dot-Spin Single-Photon Interface. *Phys. Rev. Lett.* **2010**, *105*, 033601. [CrossRef]
47. Young, A.B.; Oulton, R.; Hu, C.Y.; Thijssen, A.C.T.; Schneider, C.; Reitzenstein, S.; Kamp, M.; Höfling, S.; Worschech, L.; Forche, A.; et al. Quantum-dot-induced phase shift in a pillar microcavity. *Phys. Rev. A* **2011**, *84*, 3785–3794. [CrossRef]
48. Kimble, H.J. The Quantum Internet. *Nature* **2008**, *453*, 1023–1030. [CrossRef] [PubMed]
49. Yao, W.; Liu, R.B.; Sham, L.J. Theory of control of spin/photon interface for quantum networks. *Phys. Rev. Lett.* **2005**, *95*, 030504. [CrossRef]
50. Dmitriev, V.G.; Gurzadyan, G.G.; Nikogosyan, D.N. *Handbook of Nonlinear Optical Crystals*, 3rd ed.; Springer: Berlin/Heidelberg, Germany, 2013.
51. Fang, X.Y.; Kuang, Z.; Chen, P.; Yang, H.; Li, Q.; Hu, W.; Zhang, Y.; Xiao, M. Examining second-harmonic generation of high-order Laguerre-Gaussian modes through a single cylindrical lens. *Opt. Lett.* **2017**, *42*, 4387–4390. [CrossRef]
52. Courtial, J.; Padgett, M.J. Performance of a cylindrical lens mode converter for producing Laguerre–Gaussian laser modes. *Opt. Commun.* **1999**, *159*, 13–18. [CrossRef]
53. Niu, S.; Wang, S.; Ababaike, M.; Yusufu, T.; Miyamoto, K.; Omatsu, T. Tunable near-and mid-infrared (1.36–1.63 μm and 3.07–4.81 μm) optical vortex laser source. *Laser Phys. Lett.* **2020**, *17*, 045402. [CrossRef]